SCIENCE CHINA
Chemistry

• ARTICLES •
• SPECIAL TOPIC • Chemistry from Chinese Female Chemists

March 2015 Vol.58 No.3: 400–410
doi: 10.1007/s11426-015-5333-x

Enhanced release of the poorly soluble drug itraconazole loaded in ordered mesoporous silica

Xiao Liu & Shunai Che*

State Key Laboratory of Metal Matrix Composites; School of Chemistry and Chemical Engineering, Shanghai Jiao Tong University, Shanghai 200240, China

Received November 10, 2014; accepted November 29, 2014; published online January 20, 2015

It is known that the energy of the amorphous state of itraconazole loaded in ordered mesoporous materials is high relative to that of the crystalline state and is responsible for enhanced solubility and dissolution rate. We investigated the effects of particle size (0.7–5 μm), mesostructure (2D *p6mm*, cubic *Ia*-3*d* and cubic *Fm*-3*m*) and pore size (2.2–15.4 nm) of mesoporous silicas on the release performance of itraconazole. Results indicated that the release performance was not influenced by the particle sizes tested here, that the release performance increased with increasing pore diameter due to the lower probability of drug molecules colliding to recrystallize in large pores, and that the release performance was decreased in the cage-type pore structure (*Fm*-3*m*) compared to that in the cylindrical pore structures (*p6mm* and *Ia*-3*d*) because of the small entrance to the cage-like pores that retards the drug release.

itraconazole, poorly soluble, enhanced release, mesoporous silica

1 Introduction

The majority of new drug candidates emerging from drug discovery programs, such as itraconazole (ITZ), ibuprofen, carbamazepine and fenofibrate, are known to suffer from poor aqueous solubility and insufficient dissolution, which may lead to low oral bioavailability. Drugs are classified into four types according to the biopharmaceutical classification system (BCS): Class I, high solubility and high permeability; Class II, low solubility and high permeability; Class III, high solubility and low permeability; Class IV, low solubility and low permeability. Class II drugs permeate particularly well across the gastrointestinal epithelium, but poor solubility limits their absorption. If the solubility of these drugs is improved, a greater quantity of drug would be absorbed, which could significantly increase bioavailability. ITZ is a typical hydrophobic therapeutic compound that belongs to BCS Class II. This compound is a triazole antifungal agent that exhibits remarkable effects in the treatment of fungal infections. Many researchers use ITZ as a model drug for investigating enhanced dissolution. Researchers have devoted considerable effort to overcoming the dissolution problem. Several main formulation approaches, including dosage form, emulsion-based systems, cyclodextrin complexes, and nanosizing [1–3] have enhanced the dissolution of these drugs, but few of these technologies are commercially viable. Another widely investigated approach for achieving this goal is to use amorphous forms of drugs [4,5]. The high internal energy of the amorphous state relative to that of the crystalline state increases the solubility and dissolution rate of a drug, which enhances its bioavailability [5]. However, the amorphous state also has the potential to convert back to the energetically more favorable crystalline state during processing or storage. To enhance physical stability, amorphous drugs are typically formulated as dispersions in a physiologically inert carrier matrix. Although this approach, which is known as

*Corresponding author (email: chesa@sjtu.edu.cn)

the solid dispersion approach, has attracted widespread interest from formulation scientists, the number of commercialized solid carriers remains very limited.

The emergence of ordered mesoporous silica (OMS) materials [6–8] has attracted attention from scientists in various areas. The well-organized nanopores in OMS materials could serve as a reservoir to accommodate drug molecules [9]. Moreover, silica degrades to nontoxic silicic acid *in vivo* and is known to possess excellent biocompatibility. The unique properties of OMS materials render them suitable carriers for the solid dispersion approach: morphologies (spheres, fibers, platelets, films, and monoliths) [10–18], pore diameters (2–50 nm), high specific-surface areas (~1500 m^2/g), large pore volumes (up to 1.3 cm^3/g), mesostructures (lamellar, *p6mm*, *Fm*-3*m*, *Ia*-3*d*, *Pm*-3*n*, and *Fd*-3*m*) [19–23], and a silanol-containing surface that can be functionalized to modify drug release. In addition, OMS materials can be synthesized in large batches. Compared to conventional approaches, OMS-based systems offer numerous advantages such as operational convenience, low cost, improved efficiency, and reduced toxicity. Therefore, increasing interest has been directed toward OMS-based drug delivery systems [24,25]. The interest in OMS materials was initially focused on the development of slow-release formulations; however, the applicability of these materials has recently been expanded toward enhancing the dissolution of poorly soluble compounds [26]. Vallet-Regi *et al*. [27] were among the first to explore the drug-release properties of these materials in an attempt to prolong the release of ibuprofen using MCM-41 as a carrier. Charnay *et al*. [28] reported a rapid and pH-dependent release of ibuprofen from MCM-41. Mellaerts *et al*. [29] investigated the use of SBA-15 to accelerate the release of ITZ. Van Speybroeck *et al*. [30] demonstrated that encapsulation in SBA-15 can be applied as a dissolution-enhancing formulation approach for a large variety of poorly soluble drugs (carbamazepine, fenofibrate, and nifedipine, among others). The ability of mesoporous materials to enhance the solubility and dissolution rate of the incorporated drug is related to finite-size effects that prevent the drug molecules from rearranging themselves into a crystalline state [31–33]. Although research on the use of mesoporous materials in the field of drug delivery has been active, there has been a lack of systematic studies on the influence of OMS properties (e.g., particle size, pore size, and mesostructure) on drug dissolution. In addition, the majority of drug-release studies have been performed in media that contained surfactant.

In this work, we synthesized several types of OMS materials to be applied as ITZ-release systems. The ITZ was loaded into the OMS materials by adsorption from an organic solution. The loading state of the ITZ was confirmed by powder X-ray diffraction (XRD). Then the loaded sample was released in simulated gastric fluid (SGF) free of surfactant. The release profiles of ITZ loaded in OMS materials with different particle sizes, pore sizes, and porous structures were studied. First, MCM-41 and SBA-15 with different particle sizes were synthesized to study the effect of the particle size. Second, SBA-15s with different pore sizes were applied to investigate the effect of pore size. Finally, KIT-6 and FDU-12 with different structures were compared to SBA-15s with similar pore sizes to study the effect of the structure.

2 Materials and methods

2.1 Materials

Hexadecyltrimethylammonium bromide (C_{16}TABr), hexadecyltrimethylammonium chloride (C_{16}TACl), and tetraethyl orthosilicate (TEOS) were purchased from J&K Chemicals (China). P_{123} ($EO_{20}PO_{70}EO_{20}$), F_{127} ($EO_{106}PO_{70}EO_{106}$) and ITZ were purchased from Aldrich (USA). Other chemicals, including 1,3,5-trimethylbenzene (TMB), CH_2Cl_2, CH_3OH, NaOH, NaCl, KCl, HCl (aq), and NH_3 (aq), were purchased from Sinopharm (China) and used as received. Deionized water was used in all experiments.

2.2 Methods

2.2.1 Synthesis of MCM-41 with different particle sizes

Two types of MCM-41s with different particle sizes were synthesized according to Refs. [34,35]. The typical synthesis procedure for MCM-41-1 with a large particle size of ~3.5 μm width and ~5.0 μm length was as follows: 0.213 g C_{16}TABr and 1.41 g 2 mol/L NaOH were dissolved in 11.8 g deionized water. This mixture was stirred at room temperature. Then 1.218 g TEOS was added dropwise to the solution under vigorous stirring. The silica suspension was hydrothermally treated at 100 °C for 72 h. For the synthesis of MCM-41-2, which is composed of small nanoparticles with a diameter of 0.75 μm [31], 3.52 g C_{16}TACl and 2.28 mL of 1 mol/L sodium hydroxide solution were dissolved in 800 g of methanol/water (50:50, *w*/*w*) solution. Then, 1.8 g TEOS was added to the solution with vigorous stirring at 20 °C. After the addition of TMOS, the clear solution immediately turned opaque and a white precipitate formed. After 8 h of continuous stirring, the mixture was aged overnight. The resulting white powder was filtered, washed, and dried at 45 °C for 72 h. The powder was calcined in air at 550 °C for 6 h to remove the organic species.

2.2.2 Synthesis of SBA-15 with different particle sizes and different pore sizes

SBA-15 rods with various particle sizes were obtained by simply changing the HCl concentration and adding a co-solvent. The pore size was controlled by changing the hydrothermal temperature and adding TMB. In a typical synthesis procedure [36], 1.2 g triblock copolymer P_{123} was added to 60 mL of a 2.0 mol/L HCl aqueous solution, de-

noted as SBA-15-1. The mixture was stirred at 40 °C until the polymer was completely dissolved. Then 2.5 mL of TEOS was added to this solution under vigorous stirring. After 5 min of stirring, the mixture was maintained under static conditions at 40 °C for 20 h. Then the reaction mixture was transferred to an autoclave for hydrothermal treatment at 100 °C for 24 h. In addition, 1.2 g glycerol was added with 1.0 mol/L HCl to synthesize SBA-15-2 [37]. SBA-15-3 and SBA-15-4 were prepared using HCl concentrations of 1.0 and 0.5 mol/L, respectively. For the synthesis of silica materials with larger pores, the molar composition used during the synthesis was the same as for SBA-15-4, but the respective hydrothermal temperatures were increased to 150 and 130 °C to prepare SBA-15-5 and SBA-15-6. In addition, 6 g TMB was added under the conditions for SBA-15-4 to synthesize SBA-TMB. The resulting white powder was filtered, washed, and dried at 45 °C for 72 h. The powder was calcined in air at 550 °C for 6 h to remove the organic species.

2.2.3 Synthesis of KIT-6

In a typical synthesis [38], 6 g of P_{123} was dissolved in 217 g distilled water and 11.8 g conc. HCl (35%). To this mixture, 6 g butanol was added under stirring at 35 °C. After 1 h of stirring, 12.9 g TEOS was added at 35 °C. The mixture was stirred for 24 h at 35 °C and subsequently heated for 24 h at 130 °C under static conditions in a closed polypropylene bottle. The resulting solid product was filtered and dried at 100 °C without washing. The template was removed by extraction in an ethanol-HCl mixture, followed by calcination at 550 °C.

2.2.4 Synthesis of FDU-12

In a typical synthesis [32], 2.0 g triblock copolymer F_{127}, 2.0 g TMB, and 5.0 g KCl were dissolved in 120 mL of 2 mol/L HCl and stirred for 24 h. TEOS (8.3 g) was added to the resulting reaction mixture, which was stirred for an additional 24 h at 40 °C before being transferred to an autoclave and heated at the desired temperature for 72 h. The solid product was collected by filtration and dried at room temperature in air. The resulting silica/surfactant composite powder was calcined at 550 °C for 6 h to obtain mesoporous silica.

2.2.5 Drug loading and release

First, 20 mg calcined OMS powder was impregnated in 1.5 mL of a 4 mg/mL ITZ solution in methylene chloride sealed with plastic wrap. The mixture was stirred for 24 h under ambient conditions. Subsequently, the solvent was removed by evaporation and the powder was dried overnight at 40 °C. The release performance of ITZ from OMS was investigated at 37 °C in SGF (0.1 mol/L HCl containing 0.2 wt% NaCl). Ten mg of the loaded materials was added to a test tube containing 40 mL SGF. The tube was gently agitated at 37 °C using a rotary mixer. At desired time intervals, 1 mL release medium was withdrawn and filtered over a 0.22 μm nylon membrane filter (Rephile, China) for UV measurements and replaced with an equal volume of fresh, prewarmed medium. The ITZ release performance of the loaded OMS was compared to that of corresponding pure crystalline drugs. All of the experiments were performed for 24 h and were repeated three times. The amount of ITZ in the release medium was determined from its characteristic absorption peak in the UV spectrum.

2.3 Characterization

XRD patterns were recorded on a Rigaku (Japan) D/MAX-2200/PC X-ray diffractometer using Cu-Kα radiation (40 kV, 30 mA) at a rate of 0.5°/min over 0.6°–6° (2θ) and 5°/min over 5°–45° (2θ). The morphologies of the mesoporous materials were observed using a scanning electron microscope (SEM, JEOL JSM-7401F, Japan) with an accelerating voltage of 1.0 kV. N_2 adsorption-desorption isotherms were measured at −196 °C with a Quantachrome QUADRASORB SI Analyzer (USA). The pore-size distribution was calculated using the Barrett-Joyner-Halenda (BJH) method according to the desorption branch of the isotherm. The concentration of drug molecules in solution was measured using a UV-Vis double-beam spectrophotometer (Persee, TU-1810DPC, China).

3 Results and discussion

It is known that the enhanced release in the OMS system is due to the amorphous state of ITZ when loaded in the mesoporous materials [29,39,40]. As shown in Scheme 1, the crystalline ITZ was first dissolved in the organic solvent in the form of molecules. Then OMS was impregnated in the ITZ solution. After removal of the solvent by evaporation, the molecules are confined in the mesopores, which prevents them from converting back to the crystalline state. When these loaded materials are placed in the release medium, the adsorbed ITZ molecules will be effectively desorbed from the pore surface by competitive adsorption with water molecules because of the hydrophilicity of the silica pore walls, followed by rapid diffusion into the bulk medium.

3.1 Influence of particle size

3.1.1 MCM-41

Several properties of the OMS material may affect the release performance of the loaded ITZ, including the particle size, pore size, and mesostructure. First, to investigate the effect of internal diffusion of ITZ in the release process, we synthesized two types of MCM-41s with different particle sizes and with the smallest pore size tested in this work (Figure 1). As shown in Figure 1(a), MCM-41-1 exhibits a

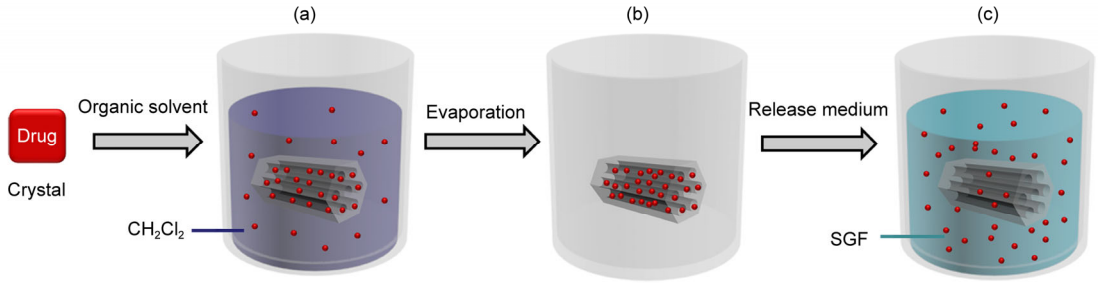

Scheme 1 Schematic representation of the ITZ loading and release process. (a) The crystalline drug is dissolved in CH_2Cl_2 in the form of molecules, and OMS is soaked in the solution; (b) CH_2Cl_2 is removed by evaporation; subsequently, the molecules are confined in the mesopores in the amorphous state; (c) in SGF, the ITZ loaded in OMS effectively diffuses into the bulk medium.

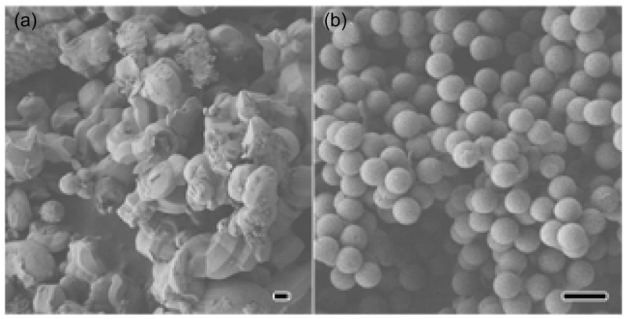

Figure 1 SEM images of two types of MCM-41 with different particle sizes. (a) MCM-41-1 with a large particle size; the molar composition used in the synthesis is C_{16}TABr:NaOH:TEOS:H_2O=1:4.48:10:1240; (b) MCM-41-2 with a small particle size; the molar composition used in the synthesis is C_{16}TACl:NaOH:TEOS=3.8:1:3.3 in a methanol/water (50:50, *w*/*w*) solution. The scale bar is 1 μm.

rodlike morphology with a width of ~2.5 μm and a length of ~5.0 μm. MCM-41-2 (Figure 1(b)) is composed of monodispersed spherical particles with a diameter of ~0.75 μm; this is the smallest among the OMS materials used here.

The small-angle XRD patterns of the two types of MCM-41s are shown in Figure 2(A). The three diffraction peaks of both MCM-41-1 and MCM-41-2 in the region of 2θ=2°–6° are indexed to the 10, 11, and 20 reflections, which corresponds to an ordered 2D hexagonal (*p6mm*) mesostructure. As shown in Figure 2(B), the nitrogen sorption isotherms of both MCM-41-1 and MCM-41-2 can be classified as Type IV. At the adsorption branches, a fairly linear increase in the absorbed volume at low pressures is followed by a steep increase in nitrogen uptake at relative pressures of $0.3<P/P_0<0.5$ for MCM-41-1 and $0.16<P/P_0<0.30$ for MCM-41-2, which is due to capillary condensation inside the mesopores. Figure 2(C) presents the pore size distribution curves obtained by applying the equilibrium model of the BJH method on the desorption branches of the nitrogen isotherms. The pore size is 2.7 nm for MCM-41-1 and 2.2 nm for MCM-41-2.

The texture properties of the two samples are summarized in Table 1. These two types of MCM-41 possess the same mesostructure and similar pore size but different particle size. Therefore, we applied these materials as carriers in the ITZ release system to study the influence of the particle size on the release performance. Commercial silica (Aerosil) composed of nonporous nanospheres with a diameter of ~40 nm (see Figure S1 for the morphology and

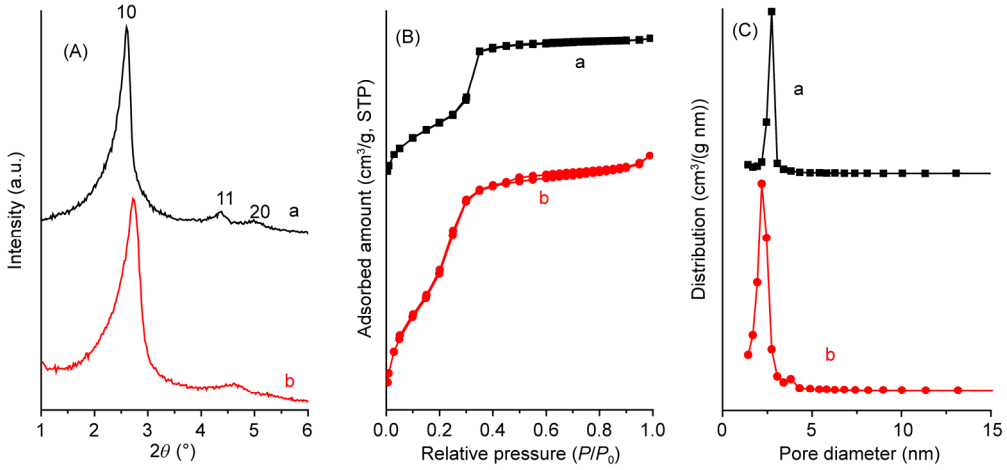

Figure 2 Small-angle XRD patterns (A), N_2-sorption isotherms (B), and pore-size distribution curves (C) of the samples shown in Figure 1. (a) MCM-1; (b) MCM-2.

Table 1 Physical properties of MCM-41 with different particle sizes

OMS	MCM-41-1	MCM-41-2
Morphology	Rod	Sphere
Particle size (μm)	2.5 width, 5 length	0.75 diameter
Mean pore size (nm)	2.7	2.2
Structure	*p6mm*	*p6mm*
Specific surface area (m^2/g)	709	1061
Pore volume (cm^3/g)	1.051	0.959

detailed texture properties, Supporting Information online) was applied for comparison.

ITZ was loaded into the calcined OMS by adsorption from an organic solution. The ITZ content is 23 wt%, which is less than the template content in the as-synthesized silica (50 wt%, the calcined OMS used here was approximately 50 wt% of the corresponding as-synthesized silica). After the loading procedure, the ITZ state was characterized by XRD through comparison with crystalline ITZ (Figure 3). The XRD pattern of crystalline ITZ (Figure 3(a)) shows characteristic high-intensity diffraction peaks at 2θ values of 14°, 17°, and 20°, which correspond to the known powder-diffraction patterns of pure crystalline ITZ [41]. ITZ-loaded Aerosil (Figure 3(b)) exhibits a weak peak at a 2θ value of 17°, which indicates that a small amount of ITZ exists in the crystalline form after loading in Aerosil, whereas the ITZ-loaded MCM-41-1 (Figure 3(c)) and MCM-41-2 (Figure 3(d)) do not present any characteristic diffraction peaks for the crystalline form of ITZ. This result demonstrates that the ITZ in MCM-41-1 and MCM-41-2 is in a completely amorphous state. Hence, the mesopores in OMS serve as a better reservoir for accommodating ITZ molecules than does Aerosil (non-porous), which indicates that OMS is an excellent ITZ carrier. The broad peaks from the loaded materials at the 2θ value of approximately 23° are caused by the amorphous silica.

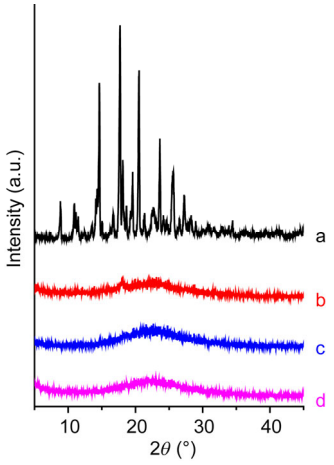

Figure 3 Wide-angle XRD patterns of pure crystalline ITZ (a); drug-loaded samples, ITZ-Aerosil (b); ITZ-MCM-41-1 (c); and ITZ-MCM-41-2 (d).

To study the effect of particle size on the poorly soluble drug-release system, the release performance of ITZ-loaded OMS was assessed using SGF at pH 1.2. The release profile of ITZ from MCM-41 is compared with those from Aerosil and crystalline ITZ (Figure 4). Crystalline ITZ did not dissolve until 10 h, demonstrating its poor solubility (Figure 4(a)). After 0.5 h, ITZ-Aerosil (Figure 4(b)), ITZ-MCM-41-1 (Figure 4(c)), and ITZ-MCM-41-2 (Figure 4(d)) released ca. 11%, 32%, and 31% of their initial ITZ content, which respectively increased to ca. 13%, 37%, and 37% after 4 h. Clearly, all of these ITZ-loaded silicas exhibited considerably faster initial release rates than the crystalline ITZ. This result confirms that the OMS-based system leads to an enhanced release of ITZ, which is caused by the amorphous state loaded in silica [29]. ITZ-loaded MCM-41-1 and MCM-41-2 exhibited better enhancement than ITZ-Aerosil, which is consistent with the XRD result (Figure 3) and thereby confirmed the advantage of OMS in the poorly soluble drug-release system. The release performance of ITZ-MCM-41-1 was similar to that of ITZ-MCM-41-2, which indicated that the particle size of the carriers does not have an obvious impact on the enhancement. In addition, the amounts of drug released did not reach 100%, likely because some ITZ molecules may have been recrystallized during collisions that occurred when they exited the mesopore surface during the release procedure. In summary, the OMS-based release system exhibits significantly enhanced release performance compared with crystalline ITZ. MCM-41 exhibits a better enhancement than the non-porous silica, and the particle size (ranging from 0.7 μm in diameter to 2.5 μm width and 5 μm length) of the carriers does not affect the ITZ release behavior.

3.1.2 SBA-15

To determine the influence of inner diffusion, we synthesized SBA-15s with different particle sizes by changing the HCl concentration and applied these materials in the release system. Figure 5 presents SEM images of rodlike SBA-15s

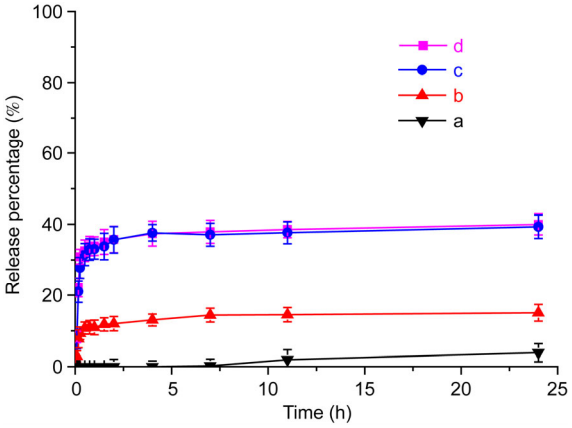

Figure 4 The release profiles of the samples shown in Figure 1. (a) Crystalline ITZ; (b) Aerosil; (c) MCM-41-1; (d) MCM-41-2.

with different particle sizes. The lengths of these samples increased from ~0.95, ~1.0, and ~3.5 to ~4.5 μm and their diameters changed from ~0.2, ~1.0, and ~0.3 to ~0.9 μm with decreasing concentration of HCl and with the addition of glycerol (Figure 5).

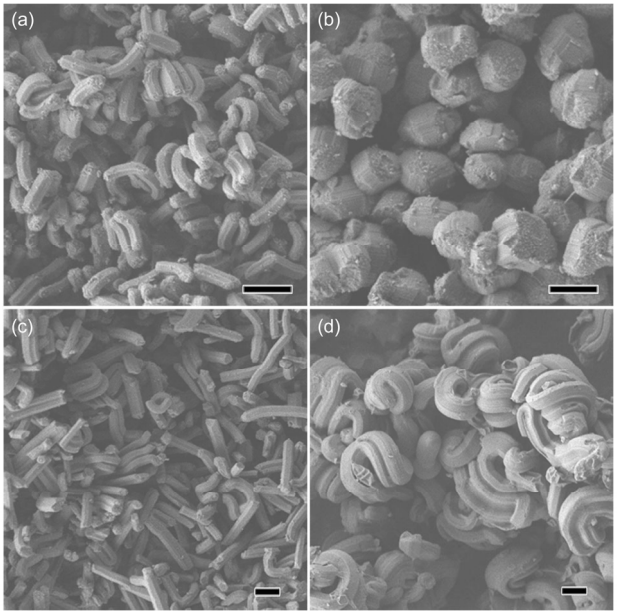

Figure 5 SEM images of SBA-15 with different particle sizes. (a) SBA-15-1; (b) SBA-15-2; (c) SBA-15-3; (d) SBA-15-4. The molar composition used in the synthesis is P_{123}:HCl:TEOS:H_2O:Glycerol=1:*x*:52:15700:*y*, where *x*=580, *y*=0 (a); *x*=290, *y*=6 (b), *x*=290, *y*=0 (c), *x*=140, *y*=0 (d). The scale bar is 1 μm.

The small-angle XRD patterns (Figure 6(A)) of these calcined samples show three well-resolved diffraction peaks in the region of 2θ=0.8°–2.2°, which can be assigned to (10), (11), and (20) associated with a well-ordered structure with *p6mm* symmetry. As shown in Figure 6(B), the nitrogen-sorption isotherms of all of the samples are Type IV with an H1-type hysteresis loop at relative pressures of 0.6–0.8, which is characteristic of mesoporous materials with cylindrical channels. Figure 6(C) presents the pore-size distribution curves of the four types of SBA-15s. The pore sizes calculated from the desorption branches of the nitrogen-sorption isotherms were very close to each other, approximately 6.5 nm.

The texture properties of the four samples are summarized in Table 2. The amorphous states of ITZ loaded in these four types of SBA-15s were confirmed by XRD (Figure S2).

The release profiles of the four types of SBA-15s are shown in Figure 7. These four types of SBA-15s, which possess a large pore size, exhibited release performance similar to that of MCM-41. After 0.5 h, these SBA-15s released ca. 52% of their initial ITZ content. After 4 h, the release percentage increased to ca. 55%. The four types of ITZ-loaded SBA-15s also exhibited faster initial release

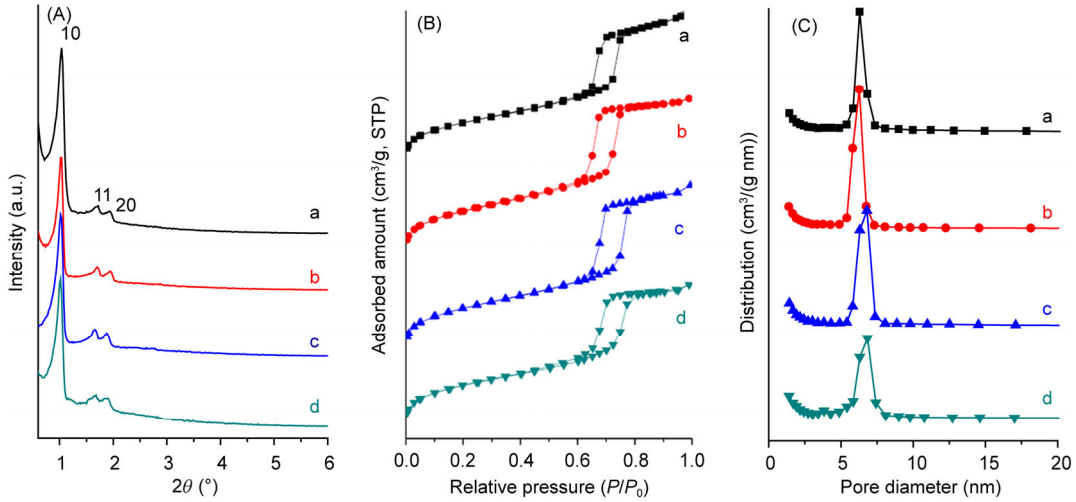

Figure 6 Small-angle XRD patterns (A), N_2-sorption isotherms (B) and pore-size distribution curves (C) of the samples shown in Figure 5. (a) SBA-15-1; (b) SBA-15-2; (c) SBA-15-3; (d) SBA-15-4.

Table 2 Physical properties of the SBA-15s shown in Figure 5

OMS	SBA-15-1	SBA-15-2	SBA-15-3	SBA-15-4
Morphology	Rod	Rod	Rod	Warped rod
Particle size (μm)	0.95 width, 0.2 length	1.0 width, 1.0 length	3.5 width, 0.3 length	4.5 width, 0.9 length
Mean pore size (nm)	6.2	6.2	6.7	6.8
Structure	*p6mm*	*p6mm*	*p6mm*	*p6mm*
Specific surface area (m^2/g)	733	798	831	774
Pore volume (cm^3/g)	1.11	0.80	1.17	1.00

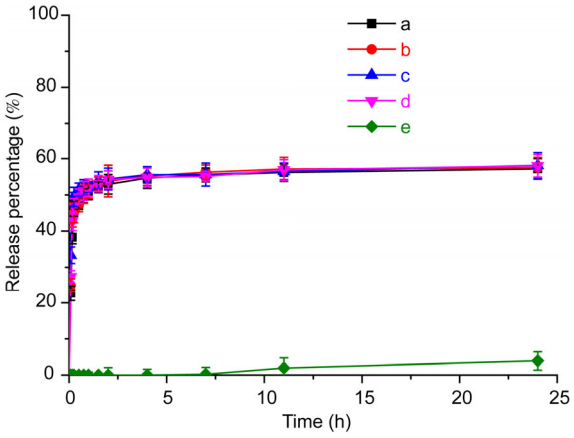

Figure 7 Release profiles of the ITZ-loaded SBA-15s. (a) SBA-15-1; (b) SBA-15-2; (c) SBA-15-3; (d) SBA-15-4; (e) crystalline ITZ.

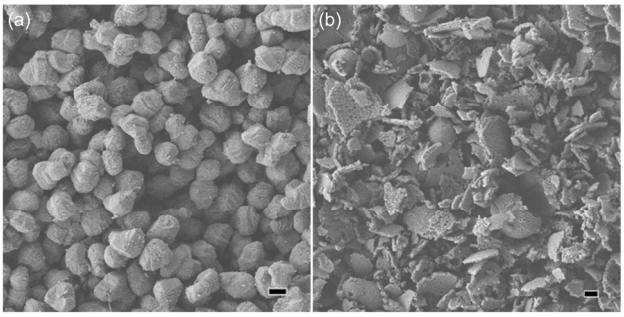

Figure 8 SEM images of two types of OMS materials with large pore sizes. (a) SBA-15-5 synthesized at 150 °C, the molar composition used in the synthesis is P_{123}:HCl:TEOS:H_2O=1:145:52:15700; (b) SBA-TMB, the molar composition used in the synthesis is P_{123}:TMB:HCl:TEOS:H_2O= 1:238:145:52:15700. The scale bar is 1 μm.

rates than the crystalline ITZ. The amount of ITZ released from the four types of ITZ-SBA-15s also did not reach 100%, which was a result of recrystallization during the release procedure or some ITZ in the crystalline state present in the surface of the OMS materials. Therefore, the size of the cylindrical channel in SBA-15 (0.95–4.5 μm length and 0.2–1.0 μm width) does not affect the ITZ release behavior.

3.2 Influence of pore size

The above results indicate that SBA-15-1 with a larger pore size exhibits a faster initial release rate and a higher release percentage compared to MCM-41-1. To investigate the effect of pore size on the enhancement, we synthesized silica materials with larger pore sizes (SBA-15-5 and SBA-TMB) by changing the hydrothermal temperature or adding TMB and applied these materials in the release system. SBA-15-5 (Figure 8(a)) is composed of rodlike nanoparticles with widths of ~1.2 μm and lengths of ~2.0 μm. The morphology of SBA-TMB (Figure 8(b)) consists of sheetlike flakes with diameters of 1.0–3.5 μm. The particle sizes of these two types of OMS are within the range without a particle size effect.

The XRD pattern (Figure 9(A)) of SBA-15-5 (Curve a) shows three typical peaks of the *p6mm* structure, whereas that of SBA-TMB (Curve b) does not show any obvious peaks due to its large unit-cell parameter. The nitrogen-sorption isotherms (Figure 9(B)) of both samples are Type IV with an H1-type hysteresis loop at relative pressures of 0.7–0.9 for SBA-15-5 and 0.8–1.0 for SBA-TMB, respectively. These results indicate that both SBA-15-5 and SBA-TMB possess cylindrical pores. The pore sizes calculated from the desorption branches are 10.0 nm for SBA-15-5 and 15.4 nm for SBA-TMB.

The texture properties of these samples are summarized in Table 3. We introduced these large-pore OMS materials into the drug-release system to study the influence of the pore size on the release enhancement. The amorphous state

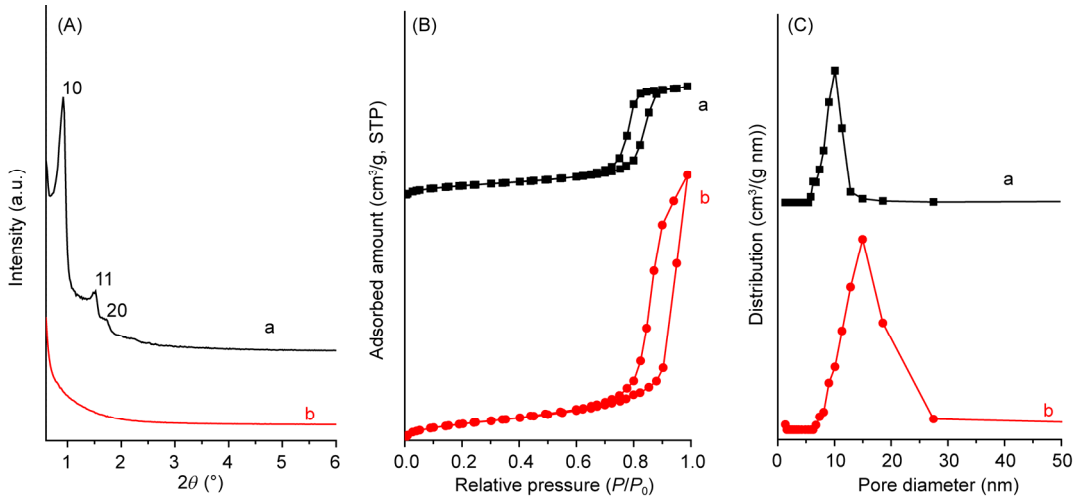

Figure 9 Small-angle XRD patterns (A), N_2-sorption isotherms (B), and pore-size distribution curves (C) of the samples shown in Figure 8. (a) SBA-5; (b) SBA-TMB.

Table 3 Physical properties of SBA-15-5 and SBA-TMB

OMS	SBA-15-5	SBA-TMB
Morphology	Rod	Flake
Particle size (μm)	1.2 width, 2 length	1–3.5 diameter
Mean pore size (nm)	10.0	15.4
Structure	*p6mm*	–
Specific surface area (m^2/g)	605	622
Pore volume (cm^3/g)	1.33	2.12

after the loading procedure is confirmed by XRD (Figure S3).

We compared the release performance of ITZ from the SBA-15-5 and SBA-TMB with that from MCM-41-1 and SBA-15-5. All of these OMS materials possess cylindrical pores but different pore sizes. As shown in Figure 10, ITZ-SBA-TMB, ITZ-SBA-5, ITZ-SBA-1, and ITZ-MCM-41-1 released 60%, 59%, 52%, and 32% at 0.5 h, respectively. At 4 h, the release percentages for these four OMS materials reached 64%, 62%, 55%, and 37%, respectively. The OMS material with the largest pore size clearly exhibited a faster initial release rate and higher release amount. The order of the initial release rate from the loaded OMS is related to the pore size. Therefore, for cylindrical pores, larger pore size (ranging from 2.2 to 15.4 nm) may lead to better enhancement in the release system. The difference in the initial release rate may be explained as follows: during the release procedure, the molecules released from mesopores are more likely to collide to recrystallize in smaller pores. As we can image, the drug molecules release quickly from mesopores. Compared to large mesopores, the channels of small pores are narrow; this increases the possibility of the released molecules colliding. Because collision will lead to a higher possibility of recrystallization, less ITZ may exist in the amorphous state. It leads to less amorphous drug releases from small pores, which slows the release rate. In addition, comparing the release profiles of ITZ-SBA-TMB and ITZ-SBA-5, ITZ-SBA-TMB releases 2% more drug than ITZ-SBA-5. An OMS material with a pore size larger than 10 nm does not lead to a significant enhancement. This result indicates that an OMS material with a pore size larger than 15.5 nm may not result in a greater enhancement than SBA-TMB.

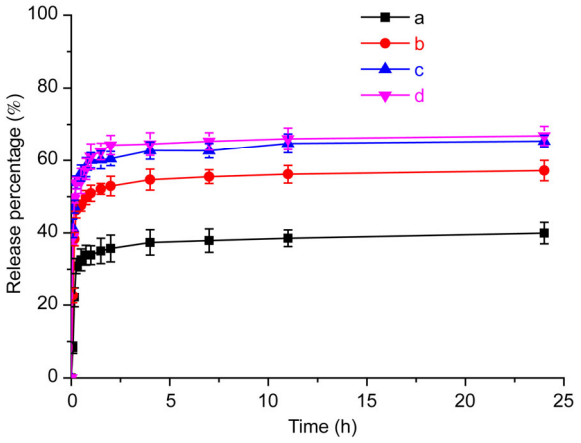

Figure 10 Release profiles of ITZ from samples. (a) MCM-41-1; (b) SBA-15-1; (c) SBA-15-5; (d) SBA-TMB.

3.3 Influence of the structure of OMS

To determine the effect of the mesostructure on the ITZ release performance, we synthesized KIT-6 with a cubic *Ia*-3*d* structure and FDU-12 with a cubic *Fm*-3*m* structure. We compared the release performance of these two materials with two types of SBA-15s with similar pore sizes. Figure 11 presents SEM images of KIT-6 (a), SBA-15-6 (b), and FDU-12 (c). KIT-6 is composed of bulk particles. SBA-15-6 consists of nanoparticles with a rodlike morphology with widths of ~1.0 μm and lengths of ~2.0 μm. The FDU-12 particles are somewhat square-like with a diameter of ~6 μm, which is slightly greater than the particle size boundary used above to eliminate the inner diffusion effect.

The XRD pattern of KIT-6 (Figure 12(A), Curve a) features

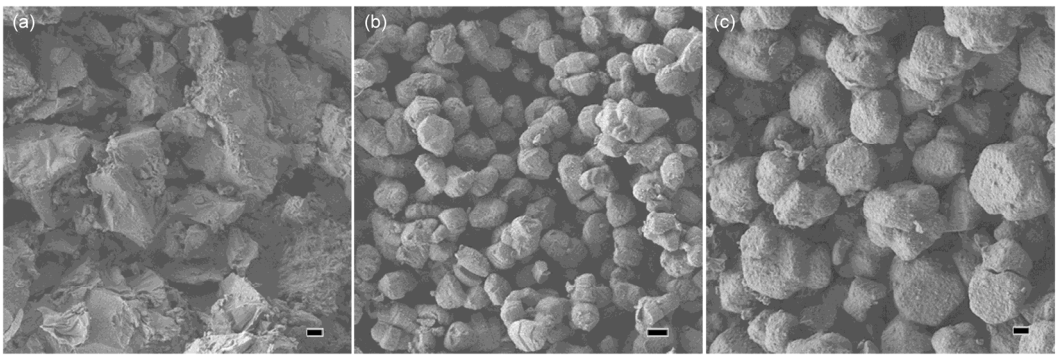

Figure 11 SEM images of OMS materials with different structures. (a) KIT-6 with a cubic *Ia*-3*d* structure, the molar composition used in the synthesis is P_{123}:butanol:HCl:TEOS:H_2O=1:80:110:60:12500; (b) SBA-15-6 with a 2D *p6mm* structure, the molar composition used in the synthesis is P_{123}:HCl:TEOS:H_2O=1:145:52:15700, synthesized at 130 °C; (c) FDU-12 with a cubic *Fm*-3*m* structure, the molar composition used in the synthesis is TMB:KCl:HCl:TEOS:H_2O=1:4:15:2.5:412 in the presence of F_{127}. The scale bar is 1 μm.

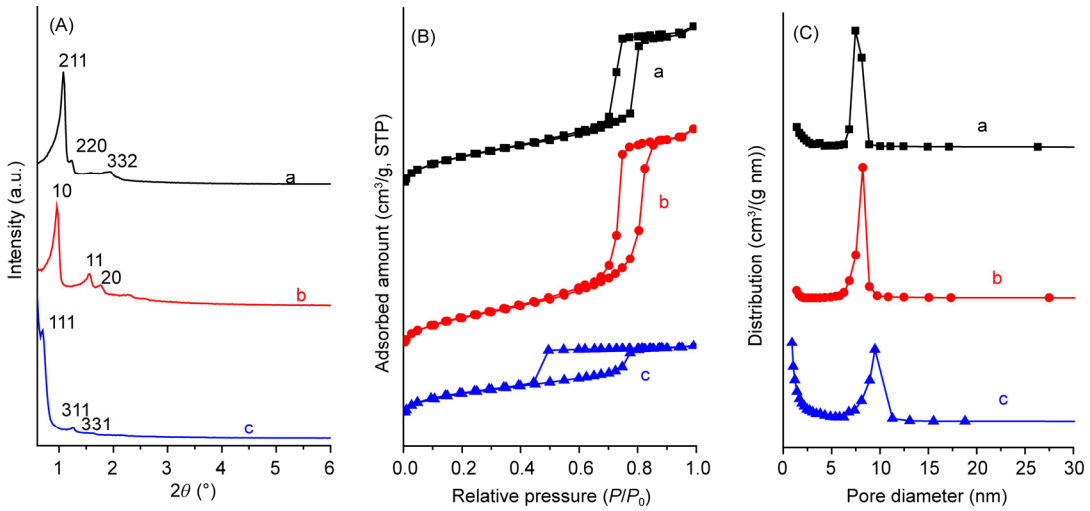

Figure 12 Small-angle XRD patterns (A), N_2-sorption isotherms (B), and pore-size distribution curves (C) of the samples shown in Figure 11. (a) KIT; (b) SBA-6; (c) FDU.

three peaks in the region of 2θ=1°–2°, which are indexed to the (211) (220) and (332) diffraction peaks for a bicontinuous cubic space group (*Ia*-3*d*). The XRD pattern of SBA-15-6 (Curve b) exhibits three typical peaks for a *p6mm* structure, and that of FDU-12 (Curve c) shows several well-resolved peaks in the region of 2θ=0.5°–2°, which can be indexed to the (111), (311), and (331) reflections of a cubic *Fm*-3*m* structure. As shown in Figure 12(B), the nitrogen-sorption isotherms obtained for KIT-6 (Curve a) and SBA-15-6 (Curve b) were type IV with an H1 hysteresis loop, indicative of large cylindrical pores. The pore sizes (Figure 12(C)) calculated using the BJH method were 7.5 nm for KIT-6 and 8.2 nm for SBA-15-6, which are similar. Furthermore, a large H2 hysteresis loop appears for FDU-12 (Figure 12(B), Curve c), which demonstrates the conventional large cagelike pores. The cage possesses a cavity size of 9.5 nm as calculated from the adsorption branch, and an entrance size of 3.8 nm as calculated from the desorption branch.

The texture properties of the three samples are summarized in Table 4. The structures of both KIT-6 and FDU-12 are different from that of SBA-15, whereas the pore size of KIT-6 is similar to that of SBA-15-6; the cavity size of FDU-12 is close to that of SBA-15-5. Therefore, we compared the release performance of KIT-6 with that of SBA-15-6 and compared FDU-12 with SBA-15-5 to study the influence of the structure on the release system. The amorphous state of the loaded drug after the ITZ loading procedure is confirmed by the XRD pattern shown in Figure S4.

The release performances of these four types of OMS materials are shown in Figure 13. Notably, both KIT-6 and SBA-15-6, which possess cylindrical pores, show a similar release performance. These two samples released ca. 55% of their initial drug content after 0.5 h. The release percentage

Table 4 Physical properties of KIT-6, SBA-15-6, and FDU-12

OMS	KIT-6	SBA-15-6	FDU-12
Morphology	Bulk	Rod	Square-like
Particle size (μm)	–	1.2 width, 2 length	4 diameter
Mean pore size (nm)	7.5	8.2	9.5/3.8
Structure	*Ia*-3*d*	*p6mm*	*Fm*-3*m*
Specific surface area (m^2/g)	638	428	519
Pore volume (cm^3/g)	1.02	1.26	0.51

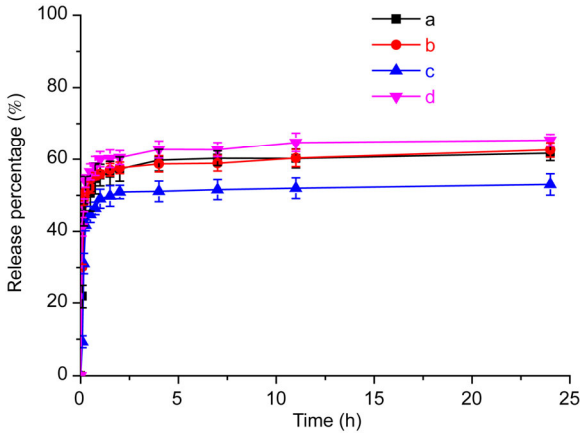

Figure 13 The release profiles of samples. (a) KIT-6; (b) SBA-15-6; (c) FDU-12 (c); (d) SBA-15-5.

reached ca. 59% after 4 h. For FDU-12 and SBA-15-5, ITZ-FDU-12 and ITZ-SBA-15-5 released ca. 48% and 59% at 0.5 h. Four hours later, the release percentages reached ca. 51% for ITZ-FDU-12 and 62% for ITZ-SBA-15-5. ITZ-FDU-12 apparently exhibits a lower release rate than ITZ-SBA-15-5, which may be caused by the different pore structures of FDU-12 and SBA-15-6. FDU-12 is composed of cagelike pores, even though its cavity size is similar to that of SBA-15-5, which may result in a release perfor-

mance similar to that of the small pore size because of the small-sized entrance that retards the enhancement. Consequently, the porous structure has an important influence in the drug- release system.

4 Conclusions

In this paper, we evaluated the effects of OMS structures on the enhancement of the ITZ release system. The control variable method was used in this work. Results indicated that MCM-41 and SBA-15, which possess similar pore sizes and structures (ranging from 0.7 μm diameter to 2.5 μm width and 5 μm length), did not influence the release performance. In comparing OMS materials with cylindrical pores but different pore sizes, we determined that larger pore size might lead to better enhancement, whereas OMS with a pore size larger than 15.4 nm may not result in greater enhancement. We also compared KIT-6 and FDU-12 with different structures to SBA-15s with similar pore sizes. The results indicated that pore type has an important influence on the drug-release system. In conclusion, these findings demonstrate that the release of ITZ from OMS materials can be tuned by varying the pore size and pore type of the carriers. OMS with cylindrical pores and pore size ~15 nm is the most appropriate carrier for ITZ.

Supporting information

The supporting information is available online at chem.scichina.com and link.springer.com/journal/11426. The supporting materials are published as submitted, without typesetting or editing. The responsibility for scientific accuracy and content remains entirely with the authors.

The authors acknowledge the support of Evonik Industries.

1 Pouton CW. Formulation of self-emulsifying drug delivery systems. *Adv Drug Delivery Rev*, 1997, 25: 47–58
2 Loftsson T, Brewster ME. Pharmaceutical applications of cyclodextrins. 1. Drug solubilization and stabilization. *J Pharm Sci*, 1996, 85: 1017–1025
3 Rabinow BE. Nanosuspensions in drug delivery. *Nat Rev Drug Discov*, 2004, 3: 785–796
4 Van Speybroeck M, Mols R, Mellaerts R, Thi TD, Martens JA, Humbeeck JV, Annaert P, Mooter GVD, Augustijns P. Combined use of ordered mesoporous silica and precipitation inhibitors for improved oral absorption of the poorly soluble weak base itraconazole. *Eur J Pharm Biopharm*, 2010, 75: 354–365
5 Hancock BC, Zografi G. Characteristics and significance of the amorphous state in pharmaceutical systems. *J Pharm Sci*, 1997, 86: 1–12
6 Yanagisawa T, Shimizu T, Kuroda K, Chuzo K. The preparation of alkyltriinethylaininonium & ndash; kaneinite complexes and their conversion to microporous materials. *B Chem Soc Jpn*, 1990, 63: 988–992
7 Zhao D, Feng J, Huo Q, Melosh N, Fredrickson GH, Chmelka BF, Stucky GD. Triblock copolymer syntheses of mesoporous silica with periodic 50 to 300 angstrom pores. *Science*, 1998, 279: 548–552
8 Beck JS, Vartuli JC, Roth WJ, Leonowicz ME, Kresge CT, Schmitt KD, Chu CTW, Olson DH, Sheppard EW. A new family of mesoporous molecular sieves prepared with liquid crystal templates. *J Am Chem Soc*, 1992, 114: 10834–10843
9 Ukmar T, Planinšek O. Ordered mesoporous silicates as matrices for controlled release of drugs. *Acta Pharmaceut*, 2010, 60: 373–385
10 Che S, Liu Z, Ohsuna T, Sakamoto K, Terasaki O, Tatsumi T. Synthesis and characterization of chiral mesoporous silica. *Nature*, 2004, 429: 281–284
11 Linton P, Alfredsson V. Growth and morphology of mesoporous SBA-15 particles. *Chem Mater*, 2008, 20: 2878–2880
12 Sayari A, Han BH, Yang Y. Simple synthesis route to monodispersed SBA-15 silica rods. *J Am Chem Soc*, 2004, 126: 14348–14349
13 Tan B, Rankin SE. Dual latex/surfactant templating of hollow spherical silica particles with ordered mesoporous shells. *Langmuir*, 2005, 21: 8180–8187
14 Linton P, Wennerstrom H, Alfredsson V. Controlling particle morphology and size in the synthesis of mesoporous SBA-15 materials. *Phys Chem Chem Phys*, 2010, 12: 3852–3858
15 Yu C, Fan J, Tian B, Zhao D. Morphology development of mesoporous materials: a colloidal phase separation mechanism. *Chem Mater*, 2004, 16: 889–898
16 Su B, Lu X, Lu Q. Oriented SBA-15-type silica films on polyimide films with laser-induced periodic microgrooves. *Langmuir*, 2008, 24: 9695–9699
17 Chen Q, Han L, Gao C, Che S. Synthesis of monodispersed mesoporous silica spheres (MMSSs) with controlled particle size using gemini surfactant. *Micropor Mesopor Mat*, 2010, 128: 203–212
18 Chen L, Zhu G, Zhang D, Zhao H, Guo M, Shi W, Qiu S. Novel mesoporous silica spheres with ultra-large pore sizes and their application in protein separation. *J Mater Chem*, 2009, 19: 2013–2017
19 Che S, Garcia-Bennett AE, Yokoi T, Sakamoto K, Kunieda H, Terasaki O, Tatsumi T. A novel anionic surfactant templating route for synthesizing mesoporous silica with unique structure. *Nat Mater*, 2003, 2: 801–805
20 Alberius PCA, Frindell KL, Hayward RC, Kramer EJ, Stucky GD, Chmelka BF. General predictive syntheses of cubic, hexagonal, and lamellar silica and titania mesostructured thin films. *Chem Mater*, 2002, 14: 3284–3294
21 Yu C, Yu Y, Zhao D. Highly ordered large caged cubic mesoporous silica structures templated by triblock PEO-PBO-PEO copolymer. *Chem Commun*, 2000, 7: 575–576
22 Ben T, Ren H, Ma S, Cao D, Lan J, Jing X, Wang W, Xu J, Deng F, Simmons JM, Qiu S, Zhu G. Targeted synthesis of a porous aromatic framework with high stability and exceptionally high surface area. *Angew Chem Int Ed*, 2009, 121: 9621–9624
23 Wei J, Wang H, Deng Y, Sun Z, Shi L, Tu B, Luqman M, Zhao D. Solvent evaporation induced aggregating assembly approach to three-dimensional ordered mesoporous silica with ultralarge accessible mesopores. *J Am Chem Soc*, 2011, 133: 20369–20377
24 Zhu L, Wang D, Wei X, Zhu X, Li J, Tu C, Su Y, Wu J, Zhu B, Yan D. Multifunctional pH-sensitive superparamagnetic iron-oxide nanocomposites for targeted drug delivery and mr imaging. *J Control Release*, 2013, 169: 228–238
25 Chen Y, Chen H, Zhang S, Chen F, Zhang L, Zhang J, Zhu M, Wu H, Guo L, Feng J, Shi J. Multifunctional mesoporous nanoellipsoids for biological bimodal imaging and magnetically targeted delivery of anticancer drugs. *Adv Funct Mater*, 2011, 21: 270–278
26 Muhammad F, Guo M, Qi W, Sun F, Wang A, Guo Y, Zhu G. PH-triggered controlled drug release from mesoporous silica nanoparticles via intracelluar dissolution of ZnO nanolids. *J Am Chem Soc*, 2011, 133: 8778–8781
27 Vallet-Regi M, Rámila A, del Real RP, Pérez-Pariente J. A new property of MCM-41: drug delivery system. *Chem Mater*, 2000, 13:

308–311
28 Charnay C, Bégu S, Tourné-Péteilh C, Nicole L, Lerner DA, Devoisselle JM. Inclusion of ibuprofen in mesoporous templated silica: drug loading and release property. *Eur J Pharm Biopharm*, 2004, 57: 533–540
29 Mellaerts R, Mols R, Jammaer JAG, Aerts CA, Annaert P, Humbeeck JV, Mooter GVD, Augustijns P, Martens JA. Increasing the oral bioavailability of the poorly water soluble drug itraconazole with ordered mesoporous silica. *Eur J Pharm Biopharm*, 2008, 69: 223–230
30 Van Speybroeck M, Barillaro V, Thi TD, Mellaerts R, Martens J, Humbeeck JV, Vermant J, Annaert P, Mooter GVD, Augustijns P. Ordered mesoporous silica material SBA-15: a broad-spectrum formulation platform for poorly soluble drugs. *J Pharm Sci*, 2009, 98: 2648–2658
31 Salonen J, Kaukonen AM, Hirvonen J, Lehto VP. Mesoporous silicon in drug delivery applications. *J Pharm Sci*, 2008, 97: 632–653
32 Fan J, Yu C, Gao F, Lei J, Tian B, Wang L, Luo Q, Tu B, Zhou W, Zhao D. Cubic mesoporous silica with large controllable entrance sizes and advanced adsorption properties. *Angew Chem Int Ed*, 2003, 115: 3254–3258
33 Alba-Simionesco C, Coasne B, Dosseh G, Dudziak G, Gubbins KE, Radhakrishnan R, Sliwinska-Bartkowiak M. Effects of confinement on freezing and melting. *J Phys: Condens Matter*, 2006, 18: R15
34 Kresge C, Leonowicz M, Roth WJ, Vartuli JC, Beck JS. Ordered mesoporous molecular sieves synthesized by a liquid-crystal template mechanism. *Nature*, 1992, 359: 710–712
35 Yano K, Fukushima Y. Particle size control of mono-dispersed supermicroporous silica spheres. *J Mater Chem*, 2003, 13: 2577–2581
36 Wang Y, Zhang F, Wang Y, Ren J, Li C, Liu X, Guo Y, Guo Y, Lu G. Synthesis of length controllable mesoporous SBA-15 rods. *Mater Chem Phys*, 2009, 115: 649–655
37 Ding Y, Yin G, Liao X, Huang Z, Chen X, Yao Y, Li J. A convenient route to synthesize SBA-15 rods with tunable pore length for lysozyme adsorption. *Micropor Mesopor Mat*, 2013, 170: 45–51
38 Kleitz F, Choi SH, Ryoo R. Cubic Ia3d large mesoporous silica: synthesis and replication to platinum nanowires, carbon nanorods and carbon nanotubes. *Chem Commun*, 2003: 2136–2137
39 Mellaerts R, Jammaer JA, Van Speybroeck M, Chen H, Humbeeck JV, Augustijns P, Mooter GVD, Martens JA. Physical state of poorly water soluble therapeutic molecules loaded into SBA-15 ordered mesoporous silica carriers: a case study with itraconazole and ibuprofen. *Langmuir*, 2008, 24: 8651–8659
40 Tozuka Y, Sasaoka S, Nagae A, Moribe K, Oguchi T, Yamamoto K. Rapid adsorption and entrapment of benzoic acid molecules onto mesoporous silica (FSM-16). *J Colloid Interf Sci*, 2005, 291: 471–476
41 Lee S, Nam K, Kim M, Jun S, Park JS, Woo JS, Hwang SJ. Preparation and characterization of solid dispersions of itraconazole by using aerosol solvent extraction system for improvement in drug solubility and bioavailability. *Arch Pharm Res*, 2005, 28: 866–874